

Geophysical Research Letters[®]



RESEARCH LETTER

10.1029/2021GL094449

Key Points:

- Tsunami source of the 2021 M_w 8.1 Raoul Island earthquake by inverting tsunami waveforms
- The main slip peaks at 5 m and is located at a depth of ~20–30 and ~100 km north of the epicenter
- New Deep-ocean Assessment and Reporting of Tsunamis network was crucial for characterizing the source and will significantly reduce the uncertainty and speed up future warnings

Supporting Information:

Supporting Information may be found in the online version of this article.

Correspondence to:





F. Romano,
fabrizio.romano@ingv.it

Citation:

Romano, F., Gusman, A. R., Power, W., Piatanesi, A., Volpe, M., Scala, A., & Lorito, S. (2021). Tsunami source of the 2021 M_w 8.1 Raoul Island earthquake from DART and tide-gauge data inversion. *Geophysical Research Letters*, 48, e2021GL094449. <https://doi.org/10.1029/2021GL094449>

Received 20 MAY 2021
Accepted 13 AUG 2021

Tsunami Source of the 2021 M_w 8.1 Raoul Island Earthquake From DART and Tide-Gauge Data Inversion

F. Romano¹ , A. R. Gusman² , W. Power², A. Piatanesi¹ , M. Volpe¹, A. Scala³, and S. Lorito¹ 

¹Istituto Nazionale di Geofisica e Vulcanologia, Roma, Italy, ²GNS Science, Lower Hutt, New Zealand, ³Department of Physics “Ettore Pancini”, University of Naples, Naples, Italy

Abstract The tsunami source of the 2021 M_w 8.1 Raoul Island earthquake in the Kermadec subduction zone was estimated by inverting the tsunami signals recorded by Deep-ocean Assessment and Reporting of Tsunamis (DART) bottom pressure sensors and coastal tide-gauges. The main asperity of up to 5 m of slip is located northeastward from the hypocenter, with features compatible with the aftershock distribution and rapid back-projection analysis. Three earthquakes of $M_w \sim 8$ or larger which also produced moderate tsunamis happened in the 20th century in the same portion of the subduction zone. This is the first great tsunamigenic event captured by the new New Zealand DART network in the South West Pacific, which proved valuable to estimate a robust image of the tsunami source. We also show a first proof of concept of the capability of this network to reduce the uncertainty associated with tsunami forecasting and to increase the lead time available for evacuation for future alerts.

Plain Language Summary We estimated the tsunami source for the 4 March 2021 Raoul Island earthquake (M_w 8.1), obtained by inverting tsunami data from tide-gauges and open ocean Deep-ocean Assessment and Reporting of Tsunamis (DART) stations. The main asperity of up to 5 m of slip is located northeastward from the hypocenter, with features compatible with the aftershock distribution and rapid back-projection analysis. This event is important because it was the strongest one of three earthquakes that occurred within hours during the same day. Moreover, it caused the largest of three tsunami that altogether represent a great test for the New Zealand DART new network. The results demonstrate the potential importance of this new DART network for resolving the tsunami source and for early warning purposes as it can reduce the uncertainty of the tsunami forecasts and at the same time increase the lead time available for evacuation.

1. Introduction

On 4 March 2021, at 19:28 UTC, a great earthquake of magnitude M_w 8.1 occurred near Raoul Island, the biggest and northernmost island of the Kermadec archipelago, New Zealand. The hypocenter (29.723°S, 177.279°W, 22 km depth; <https://earthquake.usgs.gov/earthquakes/eventpage/us7000dflf/executive>) was located along the Tonga-Kermadec portion of the subduction interface between the Australian and Pacific plates (Figure 1), locally converging at relative velocity of ~6 cm/yr (DeMets et al., 2010). The location, geometry, and mechanism along with the low dip angle of some available solution (e.g., USGS W-phase MT and Global CMT, <https://www.globalcmt.org>), point to an interplate subduction earthquake.

The subduction interface around Raoul Island is characterized by a relatively high interseismic coupling, as constrained using GPS velocities from sensors installed on this small island (Power et al., 2012). Several major-to-great earthquakes occurred to the north-east within ~200 km in the same zone since 1900 (Figure 1; Todd & Lay, 2013), with magnitude $M_w \sim 8$ or larger: the M_w 8.0–8.6 on 2 May 1917 (Lockridge & Lander, 1989; Power et al., 2012), the 14 M_w 8.0 on January 1976 (Power et al., 2012), and the M_w 7.9 on 20 October 1986 (Lundgren et al., 1989). Additionally, two intraplate events occurred within few months from each other in 2011 (Todd & Lay, 2013), with M_w 7.6 (July 6) and M_w 7.4 (October 21).

Two major earthquakes preceded the 2021 M_w 8.1 event on the same day (<https://www.usgs.gov/news/kermadec-and-new-zealand-earthquakes>); the first one (M_w 7.3) occurred ~6 h earlier (13:27 UTC) and was located ~170 km north-east of Gisborne (New Zealand); the second one (M_w 7.4) occurred ~2 h earlier (17:41 UTC) and was deeper and located just ~55 km to the west of the M_w 8.1 event. The vicinity in time

© 2021 The Authors.

This is an open access article under the terms of the [Creative Commons Attribution-NonCommercial License](https://creativecommons.org/licenses/by-nc/4.0/), which permits use, distribution and reproduction in any medium, provided the original work is properly cited and is not used for commercial purposes.

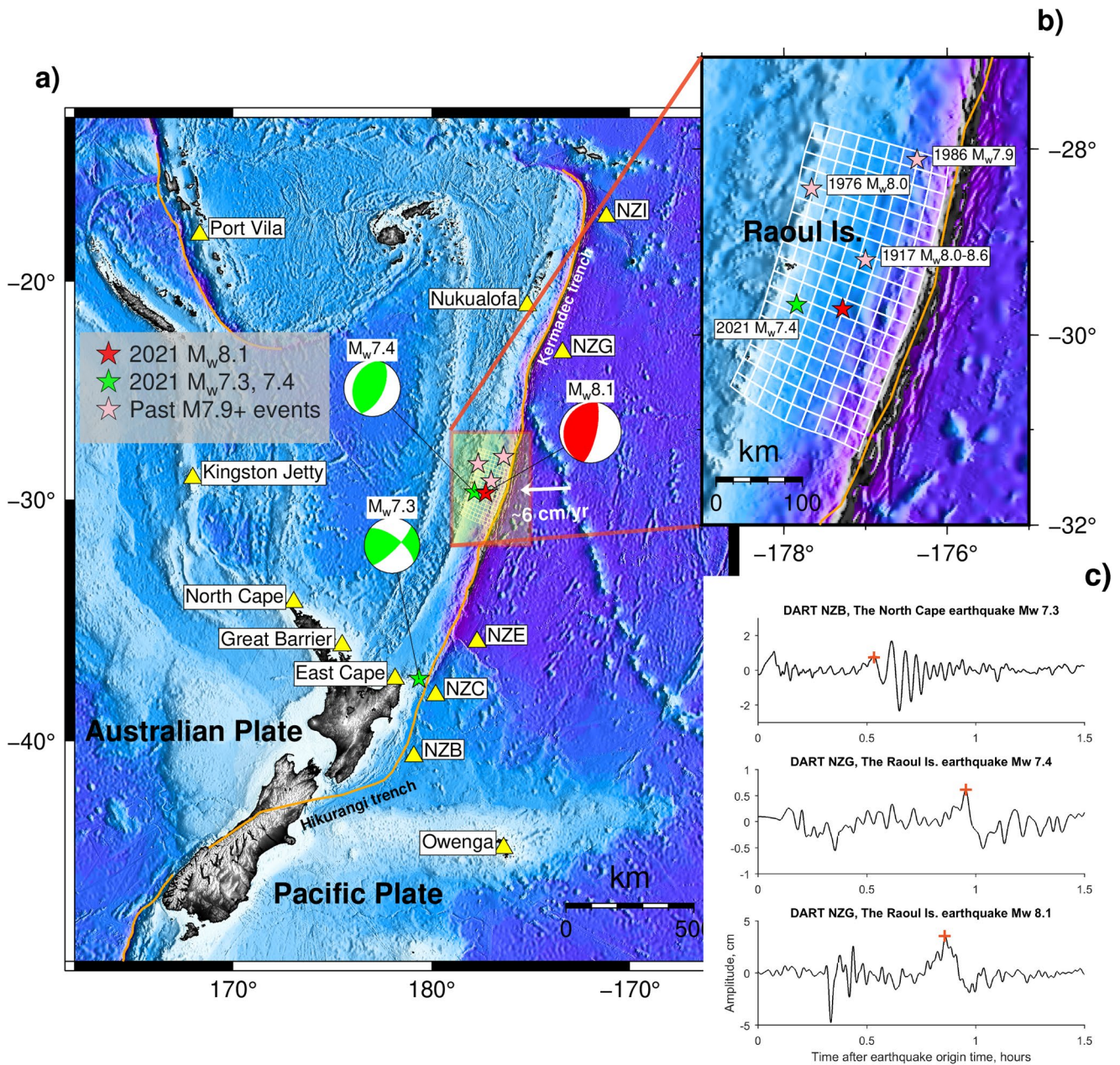


Figure 1. Location Map: The figure shows: (a) Epicenters and focal mechanism of the Raoul Island earthquake (red star and beach ball) and of the preceding earthquakes on the same day (green stars and beach balls); yellow triangles indicate the positions of tide-gauges and DARTs used in this study. (b) Pink stars represent the epicenters of the past M8+ earthquakes occurred in the same area of the 2021 event. (c) The tsunami waveforms of the 2021 North Cape earthquake (M_w 7.3) recorded at DART NZB, the 2021 Raoul Island foreshock (M_w 7.4) recorded at DART NZG, and the 2021 Raoul Island mainshock (M_w 8.1) recorded at DART NZG. Red crosses indicate the peak amplitudes of the first tsunami wave cycles.

and space between the M_w 7.4 and the M_w 8.1 events suggest that they represent an interplate earthquake doublet (Lay & Kanamori, 1980), similar to the earthquakes that occurred in 1976, and the foreshock may have perturbed the preexisting stress-state triggering the larger mainshock 2 h later.

All the three earthquakes generated moderate tsunamis, recorded by the New Zealand Deep-ocean Assessment and Reporting of Tsunamis (DART) network (Fry et al., 2020), whose installation was started in 2019 and is scheduled to be finished in 2022. This rather exceptional circumstance served to test the new network, showing its importance for real-time tsunami detection (Kornei, 2021). All the events were also recorded by several coastal tide-gauges around New Zealand (<https://www.gns.cri.nz/Home/Our-Science/Natural-Haz>

ards-and-Risks/Tsunami/ and <https://www.geonet.org.nz/tsunami>) and in the Pacific Ocean (<http://www.ioc-sealevelmonitoring.org>). In particular, the small tsunamis generated by the first two M_w 7.3 and 7.4 earthquakes were recorded by the two tide-gauges installed along the coast of Raoul Island. Unfortunately, the communications system used by these tide-gauges was damaged by the intense shaking caused by the M_w 8.1 event, and the last data sample was transmitted at about the origin time (OT) of the earthquake before the tsunami arrival. The largest tsunami wave amplitudes were measured along the southern coast of Norfolk Island (Kingston Jetty); amplitudes of ~ 15 cm were also observed along the coast of North Island in New Zealand (North Cape, Great Barrier) and Chatham Island (Owenga), whereas amplitudes < 10 cm were observed along the coasts of Tonga and Vanuatu archipelagos.

Here, we estimated the tsunami source of the 2021 M_w 8.1 Raoul Island earthquake by inverting the tsunami waveforms recorded by seven tide-gauges (in Australia, New Zealand, Tonga, and Vanuatu) and five DART buoys (Figure 1a). This is a very important step for a better understanding of the phenomenon and for constraining the hazard from future events (e.g., Gusman et al., 2015; Romano et al., 2015; Satake, 2014; Williamson et al., 2017). We adopted the methodology previously applied to several, mainly mega-thrust, tsunamigenic earthquakes (Romano, Lorito, Lay, et al., 2020; Romano, Lorito, Piatanesi, & Lay, 2020 and references therein). We also compare our source model with available faster solutions, and finally provide a first proof of concept regarding the importance of the new DART network in the context of tsunami forecasting and early warning.

2. Data and Method

2.1. Tsunami Data

We used data from seven tide-gauges and five DARTs (Figure 1a). The sampling rate for the tide-gauge waveforms is 1 min, whereas for the DARTs it is 30 s (Table S1).

The tsunami signal for each tide-gauge was obtained by removing the tidal component from the original records provided by the Intergovernmental Oceanographic Commission (IOC) Sea level Station web service; the tide filtering was performed by applying a LOWESS algorithm (Romano, Lorito, Lay, et al., 2020). For the DARTs, we first removed the tides by the polynomial fit method (Figure 1c). Then high frequency waves were removed using a low pass filter with cutoff period of 200 s to get the tsunami waveforms.

2.2. Fault Model and Green's Functions

A 3D fault geometry (with variable strike and dip angles) was built upon the SLAB2.0 subduction interface model (Hayes et al., 2018); the spatial extension was defined based on the aftershocks that occurred 2 weeks after the mainshock (USGS, <https://www.usgs.gov/natural-hazards/earthquake-hazards/earthquakes>). We ended up with 162 quadrilateral subfaults with an average size of $\sim 18 \times 18$ km² (Figure 1b; Tables S1 and S2).

The tsunami initial condition was obtained by splitting each subfault into a pair of triangles and then combining the vertical seafloor deformation associated with each triangular dislocation obtained for a homogeneous half-space (Nikkhoo & Walter, 2015); the contribution of the horizontal displacement of the oceanic slope near the trench (Tanioka & Satake, 1996); and the short wavelength filtering effect of the water column (Kajiura, 1963) were also estimated. Finally, the tsunami Green's functions were computed with the multi-GPU finite-volume Tsunami-HySEA code (de la Asunción et al., 2013; Macías et al., 2017) that solves numerically the nonlinear shallow water equations on a structured bathymetric grid; here, a two-level nested grids system was adopted; the finest grids have a resolution of 15 arc-s (SRTM15, http://topex.ucsd.edu/WWW_html/srtm30_plus.html) around the tide-gauge positions, the coarsest one including the source and the DARTs, has a spatial resolution of 1 arc-min (obtained by resampling the 15 arc-s model).

2.3. Inversion

We estimated the slip distribution (average slip and rake angle on each subfault) of the 2021 Raoul Island earthquake. The inverse problem was solved by means of the Heat-Bath version of the Simulated Annealing

(Piatanesi & Lorito, 2007; Rothman, 1986). A very large number of slip models were evaluated through a misfit function:

$$F(T) = 1 - \frac{2 \int_{t_1}^{t_2} \text{obs}(t) \text{synt}(t - T) dt}{\int_{t_1}^{t_2} \text{obs}^2(t) dt + \int_{t_1}^{t_2} \text{synt}^2(t - T) dt}, \quad (1)$$

where obs and synt represent the observed and predicted tsunami waveforms, respectively, t_1 and t_2 , represent the boundaries of the time window used to invert the data, chosen to include only the first cycles of the signal which carry most of the source information before the influence of local bathymetric features or other reflected or transformed phases may become too strong. This misfit function, proposed by Romano, Lorito, Lay, et al. (2020), minimizes the possible temporal misalignment between observed and modeled tsunami waveforms (Tsai et al., 2013; Watada et al., 2014). Positive values of T correspond to an earlier arrival of the synthetics.

The tsunami Green's functions were shifted in time from the earthquake initiation according to a circular rupture front starting from the hypocenter with an imposed velocity $V_R = 2.3$ km/s (from the USGS finite fault model, <https://www.usgs.gov/news/kermadec-and-new-zealand-earthquakes>). To prevent overfitting, the rake angle was constrained to be uniform on each of three large blocks of 6×9 subfaults, and the problem regularized by imposing a smoothing constraint and seismic moment minimization.

Due to the non-uniqueness of the solution, in place of presenting the best model corresponding to the absolute minimum of the cost function, which might represent an outlier, we preferred the average slip model. This average model was computed as the weighted mean of selected models possessing a relatively low cost function value; the weights are the inverse of the cost functions (further details in Romano, Lorito, Lay, et al., 2020).

A resolution test was performed to verify if the current fault geometry discretization and the instrumental azimuthal coverage is suitable for solving the slip distribution (details in Supporting Information S1). The results of the test (Figure S3) show that, despite an azimuthal gap in both the directions perpendicular to the strike and particularly eastward, as compared to the coverage in the along-strike direction (Figure 1), the instrumental coverage is in principle appropriate for estimating the slip distribution of the Raoul Island earthquake.

3. Results and Discussion

3.1. Tsunami Source Model

The slip distribution obtained from the inversion of real data features a predominantly unilateral rupture propagation characterized by the main patch of slip located NNE from the epicenter (Figure 2). This slip patch extends for ~ 130 km along strike and for ~ 90 km downdip with a maximum slip of ~ 5 m near 177°W , 29°S (Table S3) at a depth of ~ 20 – 30 km. Some less-intense slip also occurred up to the trench in the up-dip direction from the main patch, and also approximately southward from the epicenter. The relatively low dispersion of the marginal distributions for the slip values within the ensemble for each subfault, also centered around the average slip values (Figure S4), indicate that the coseismic dislocation along the fault surface is well resolved.

The seismic moment associated with the slip distribution in Figure 2a is $M_0 = 1.15 \times 10^{21}$ Nm, equivalent to an earthquake moment magnitude M_w 8.0 (using a rigidity of 40 GPa) and slightly smaller than the moment tensor solutions estimated by GCMT or USGS, whose moment magnitude is equal to M_w 8.1. The relatively deep position (~ 20 – 30 km) of the main slip patch resulted in a correspondingly limited seafloor deformation (maximum positive value of ~ 1.1 m, Figure 2b), thus limiting in turn the coastal impacts, despite the large earthquake magnitude. This situation is similar to the 2005 M_w 8.6 Nias-Simeulue earthquake, which also caused a small tsunami for its magnitude (Fujii et al., 2020); although for the 2005 event the fact that a significant portion of the slip occurred beneath Nias Island may also have reduced the tsunami potential of the earthquake.

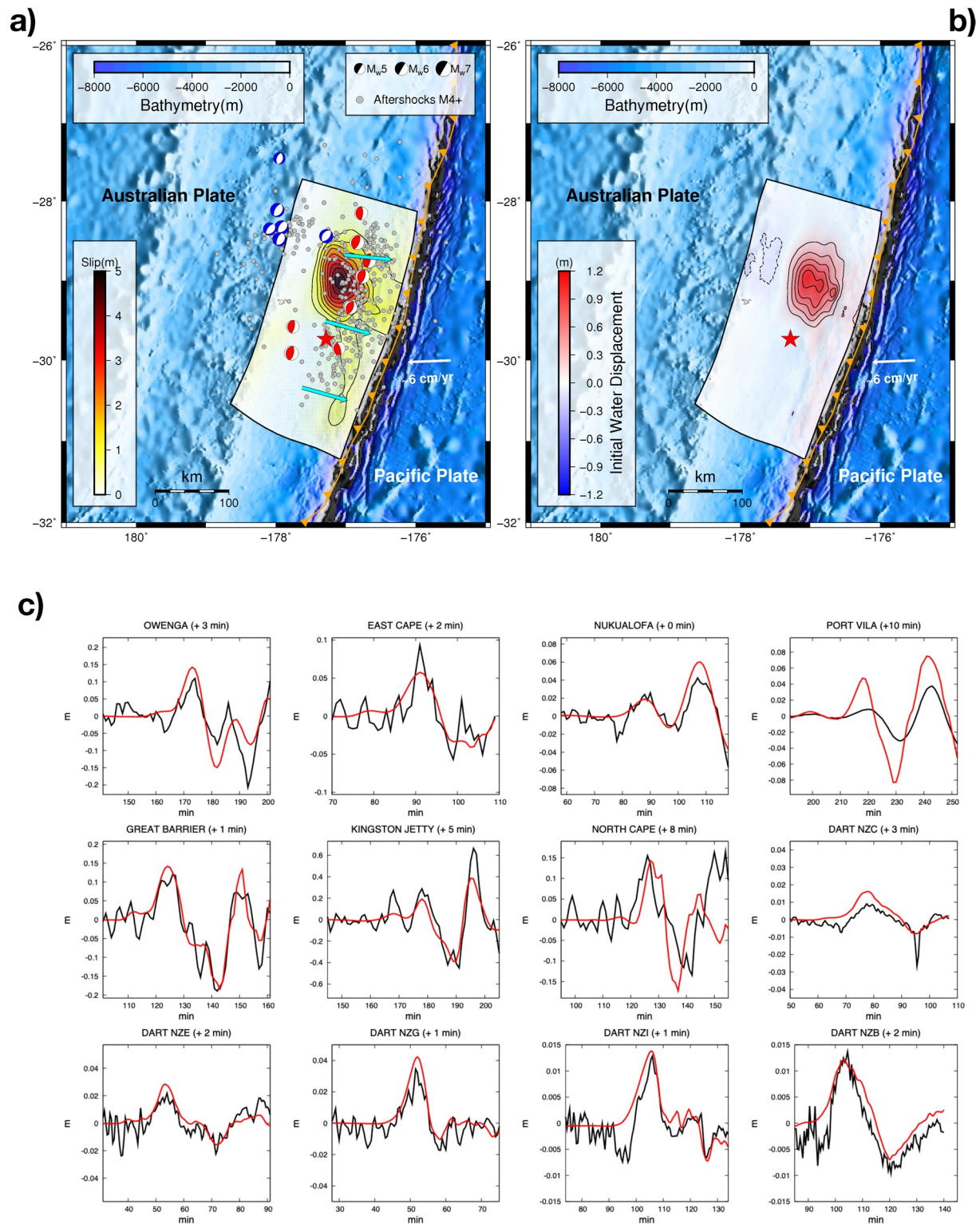


Figure 2. The 2021 Raoul Island earthquake: (a) Slip distribution (0.5 m contour line) and estimated rake (cyan arrows); gray dots represent the aftershocks (M₄+) occurring within 1 month after the mainshock; aftershocks with a thrust and normal faulting mechanism (GEOFON catalog) are shown by red and blue beach balls, respectively. (b) Tsunami initial condition: contour lines of positive (solid black) and negative (dashed black) displacement at 0.2 and 0.1 m interval. (c) Comparison between observed (black) and predicted (red) tsunami waveforms; optimal time shift estimated by OTA for each tsunami sensors are reported within the brackets.

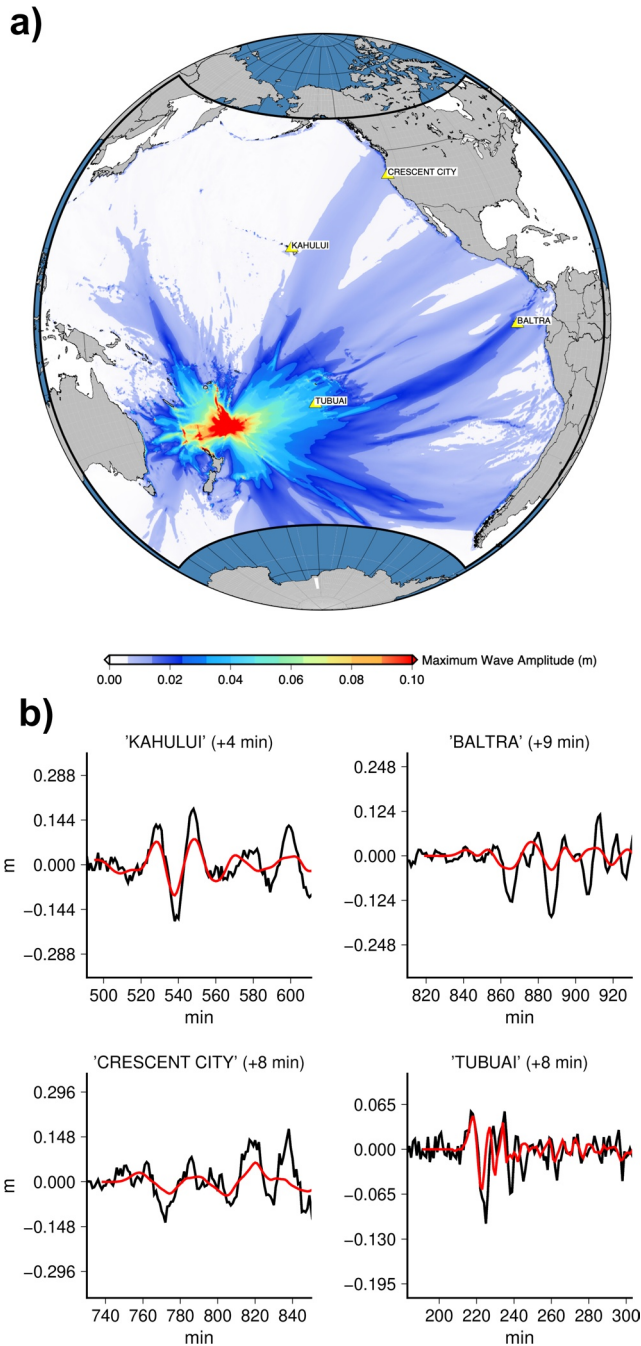


Figure 3. Raoul Island tsunami far-field propagation: (a) Tsunami maximum wave amplitudes distribution in the Pacific Ocean. (b) Comparison between the observed (black) and predicted (red) tsunami waveforms for some tide-gauges (yellow triangles).

The average rake angle ($\sim 96^\circ$, ranging from $\sim 92^\circ$ to $\sim 99^\circ$) is in agreement with both the W-phase (98°) and GCMT (96°) moment tensor solutions, and is consistent with the local plate convergence direction.

The agreement between observed and predicted tsunami waveforms is satisfactory (Figure 2c), particularly for the DARTs; a discrepancy in terms of wave amplitude is observed at some tide-gauges (the most evident at Port Vila), likely due to the inaccuracy of the bathymetry model, whereas the period is well predicted for all the sensors. The time-shift estimated (OTA) between observed and modeled tsunami waveforms at the tide-gauges is on average ~ 4 min, which is compatible with the uncertainty in the bathymetry model around the tide-gauge position (Heidarzadeh & Satake, 2014; Romano et al., 2016; Romano, Lorito, Lay, et al., 2020); the time-shift estimated for the DARTs is in the range of ~ 1 – 4% of the observed tsunami travel times (Watada et al., 2014). We also reported in Figure S5 the marginal distributions for the time-shifts estimated by the inversion. We note that these distributions are unimodal thus pointing to a single solution for the optimal time alignment, which is also the central value of the distributions.

3.2. Forward Modeling to Distant Stations

This tsunami propagated all over the Pacific Ocean. The distribution of the maximum wave amplitude during the propagation highlights how the tsunami energy, traveling eastward, “prefers” specific paths pointing toward the Austral Islands (~ 13 cm at Tubuai), the Hawaii Islands (~ 30 cm at Kahului), the US West coast (~ 20 cm at Crescent City), and the Galapagos archipelago (~ 20 cm at Baltra, Figure 3a). This feature is shared with previous tsunamigenic M8+ earthquakes that occurred in the same area in 1917, 1976, and 1986, respectively, whose tsunamis were recorded by several far-field tide-gauges with maximum amplitudes of a few tenths of centimeters (Power et al., 2012). Here, far-field data were also used to perform an independent verification of the tsunami source model obtained in this study (Figure 3b). A system of telescopic nested bathymetric grids was used around each tide-gauge from 2 to 0.25 arc-min; nevertheless, probably this maximum resolution of ~ 450 m is still not fine enough for resolving the near-gauge details as testified by a slight amplitude underestimation.

3.3. Comparison With Seismicity and Available Rapid Inversions

A preliminary finite fault model proposed by USGS (hereinafter FFM-USGS) and estimated from broadband teleseismic P, SH, and surface waveforms inversion (<https://earthquake.usgs.gov/earthquakes/eventpage/us7000dflf/finite-fault>) presented a rupture pattern with two main slip patches (Figure 4a). The main patch has a maximum slip of ~ 3.5 m and size similar to the main asperity of our model in Figure 2a, whereas its location is slightly deeper and shifted in the SSW direction. The second

slip patch in the FFM-USGS model is smaller (spatial extent of ~ 50 km both along strike and along dip) and shallower with a maximum slip of ~ 3 m; on the other hand, even though approximately in the same area, the shallow slip present in our slip model has lower values (< 2 m). We also observe that the rupture area of the foreshock (M_w 7.4) that occurred ~ 2 h earlier, estimated through a teleseismic inversion (Figure 4a, <https://earthquake.usgs.gov/earthquakes/eventpage/us7000dfk3/finite-fault>) falls outside the rupture area of the mainshock estimated in our study.

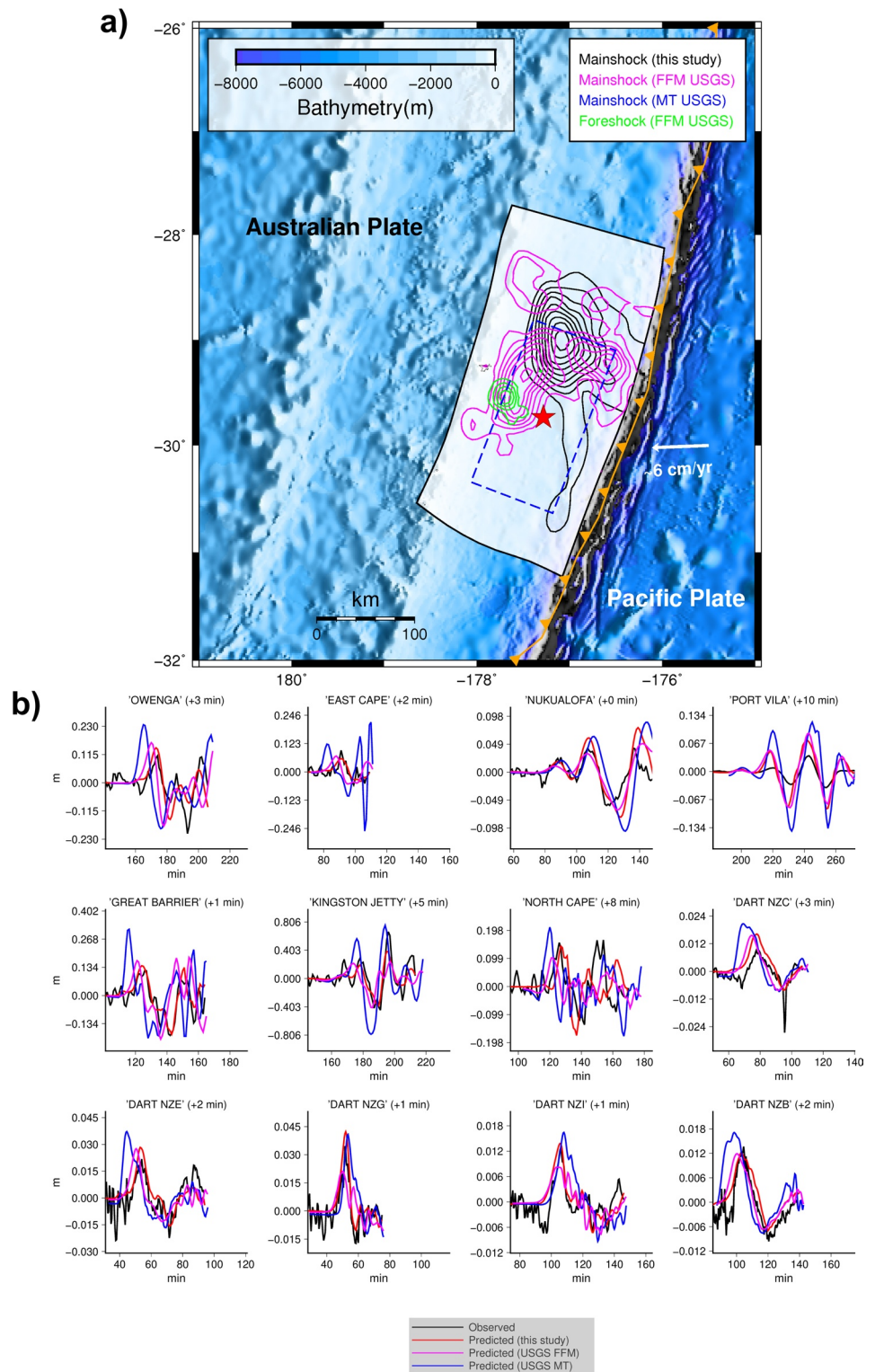


Figure 4. Comparison with other models: Comparison between our slip model (black), the USGS Finite fault models of the foreshock (green) and mainshock (magenta), and the rectangular fault (dashed blue line) built using MT-USGS parameters and earthquake empirical scaling relation; slip contour lines at 0.5 m intervals.

We performed a tsunami forward modeling using as initial condition the seafloor coseismic deformation resulting from (i) the FFM-USGS and (ii) a simpler rectangular fault derived from the USGS moment tensor solution (hereinafter MT-USGS). MT-USGS has the following parameters: strike = 201°, dip = 16°, and rake = 98° (<https://earthquake.usgs.gov/earthquakes/eventpage/us7000dflf/moment-tensor>); the fault size ($\sim 183 \times 94 \text{ km}^2$) and the average slip (3.45 m) for the MT-USGS were defined through an empirical earthquake scaling relation (Strasser et al., 2010). The tsunami signals predicted using the MT-USGS model (Figure 4b) overestimate the observed wave amplitudes. They also feature a significant early arrival for the sensors located to the south-west of the source due to the smaller mutual source-receiver distance with respect to that characterizing the main slip patch of our model (Figure 2a), even though we have corrected the tsunami arrival times for the MT-USGS prediction with the same time-shifts inferred by the OTA for our model. The FFM-USGS model produces tsunami amplitudes comparable to the ones resulting from our slip model; however, despite the time-shifts, the time-mismatch persists, likely due to the deeper and southward shifted main slip patch of the FFM-USGS model. Some difference in the spatial resolution of the slip distribution can be often observed between finite fault models obtained inverting teleseismic and tsunami data, with the former more sensitive to the temporal aspects of the seismic rupture and the latter more sensitive to the slip location (e.g., Lorito et al., 2016).

Under the assumption that the rupture has featured a simple unilateral propagation consistent with the imposed constant rupture velocity, we estimated a rupture duration of $\sim 56 \text{ s}$ to develop the main asperity in our model (Figure 2a). We did it by dividing the distance between the nucleation and the region where the slip becomes 10% of the peak slip by the rupture velocity.

This is in agreement with the moment rate estimated by teleseismic inversion and by back-projection analysis (IRIS, <https://ds.iris.edu/spud/backprojection/18822452>). Interestingly, the north-northeastward unilateral coseismic rupture propagation estimated from the tsunami data inversion is consistent with the surface projection of the radiated energy as shown by the back-projection. Furthermore, the shallow and moderate slip extending up to the trench at around 29.5°S may also explain the secondary burst of energy appearing in the back-projection between 45 and 60 s from the earthquake OT.

We observe that the M4+ aftershock locations, which occurred in the 30 days after the mainshock (from USGS catalog), are distributed roughly around the rupture area of the Raoul Island earthquake shown in Figure 2a. In particular, the large events (for which a moment tensor was calculated, data from GEOFON) are mainly distributed along the margins of the main slip patch; such a deficiency of aftershocks in the area of large coseismic dislocation is in principle in agreement with the hypothesis of stress increase in the peripheral areas of high slip regions (Wetzler et al., 2018).

3.4. Testing the Tsunami Warning Capabilities of the New DART Network

Finally, we highlight the importance of this new DART network for tsunami warning. The maximum tsunami amplitude at the first New Zealand tide-gauges is measured $\sim 90 \text{ min}$ after the earthquake OT. All other coastal tide-gauges in Australia, New Zealand, Tonga, and Vanuatu that we used for this study present later tsunami peaks. For this reason, we inverted the first 60 min of the DARTs whose peaks occur well before this time, namely the NZE and NZG stations. These two stations appear to be sufficient to predict early enough, and to an extent, that is, fully satisfactory for early warning purposes, the maximum tsunami amplitudes, and even the waveforms for all the sensors used in this study (Figure 5). Only the Kingston Jetty tide-gauge was an exception, as the signal there was underestimated, but this is likely due to unmodeled shallow bathymetry since the same underestimation is also observed in the full inversion results (Figure 2b). By including a third DART station in the inversion and extending the time window to the first 90 min, the prediction at the other stations is only slightly improved (Figure 5); however, in this case the lead time for evacuation is reduced by 30 min, and it is for example, very limited at East Cape.

The sources obtained from the inversion of two and three DARTs are reported in the Supporting Information S1 (Figure S6). It is evident that a fair source representation can be obtained with three DARTs, while, even if adequate for warning purposes, with only two DARTs the source process is not well-constrained.

As a point of reference, we also demonstrate that the forward prediction obtained using the USGS-MT (in principle the fastest available earthquake solution) systematically overestimates the amplitude of the

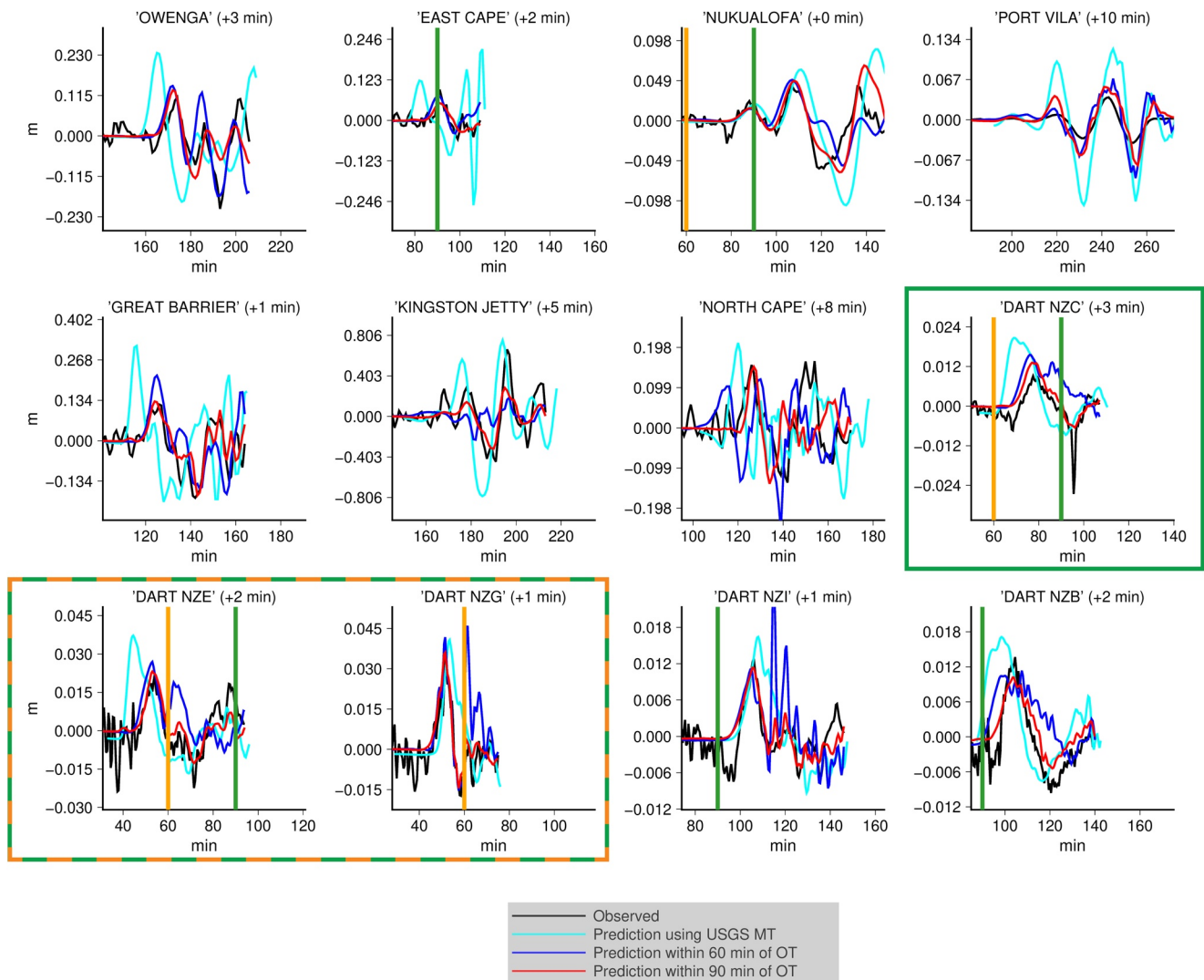


Figure 5. Experiment for tsunami forecasting: Comparison between observed (black) and predicted tsunami waveforms inverting DART data within 60 min (blue) and 90 min (red) of the OT, and by using the USGS-MT.

observed data. We point out that we did not apply phase correction to the tsunami waveforms for the USGS-MT model. While more extensive tests with different sources would be recommended, this simple test clearly highlights that the DART network is crucial not only for rapid confirmation/cancellation of tsunami warnings (Kornei, 2021), but also to reduce the uncertainty in forecasts and their associated alerts, while still guaranteeing a significant lead time for most of New Zealand North Island coastal locations and for all the considered coastal locations of the other countries.

4. Conclusions

We estimated the tsunami source of the 2021 Raoul Island earthquake by inverting tsunami waveforms recorded by several coastal tide-gauges and DART stations. The slip pattern features a mainly unilateral rupture propagation departing from the hypocenter and extending northward with a slip patch of maximum ~ 5 m. The depth of this patch explains the relatively small observed tsunami. Secondary slip occurred up to the trench zone on both sides of the epicenter. The estimated slip direction is consistent with the relative convergence direction between the Australia and Pacific plates. The rupture pattern is consistent with the aftershock distribution and the back-projection analysis. This was an important test of the new DART network in the southwest Pacific; it recorded three consecutive tsunamis and the data it recorded allowed for

an accurate reconstruction of the tsunami source, highlighting at the same time the potential for constraining real-time tsunami forecasts of future events.

Conflict of Interest

The authors declare that the research was conducted in the absence of any commercial or financial relationships that could be construed as a potential conflict of interest.

Data Availability Statement

Figures in the main text and supporting information made use of GMT (<https://www.generic-mapping-tools.org>) and MATLAB (www.mathworks.com) software. DART and tide-gauges data available on New Zealand's GeoNet (www.geonet.org.nz) and at the following link <https://figshare.com/s/887ffd3ec85498107de7>.

Acknowledgments

We thank the IOC of UNESCO (<http://www.ioc-sealevelmonitoring.org/>) for providing tsunami data. Aditya R. Gusman and William Power were supported by the New Zealand Ministry for Business, Innovation, and Employment (MBIE) Endeavour fund (Project: Rapid Characterisation of Earthquakes and Tsunami: Fewer deaths and faster recovery). We thank two anonymous reviewers for their valuable comments and suggestions. Open access funding provided by Istituto Nazionale di Geofisica e Vulcanologia within the CRUI-CARE Agreement.

References

- de la Asunción, M., Castro, M. J., Fernández-Nieto, E. D., Mantas, J. M., Acosta, S. O., & González-Vida, J. M. (2013). Efficient GPU implementation of a two waves TVD-WAF method for the two-dimensional one layer shallow water system on structured meshes. *Computers & Fluids*, *80*, 441–452. <https://doi.org/10.1016/j.compfluid.2012.01.012>
- DeMets, C., Gordon, R. G., & Argus, D. F. (2010). Geologically current plate motions. *Geophysical Journal International*, *181*(1), 1–80. <https://doi.org/10.1111/j.1365-246X.2009.04491.x>
- Fry, B., McCurrach, S.-J., Gledhill, K., Power, W., Williams, M., Angove, M., et al. (2020). Sensor Network Warns of Stealth Tsunamis. *Eos*, *101*. <https://doi.org/10.1029/2020eo144274>
- Fujii, Y., Satake, K., Watada, S., & Ho, T.-C. (2020). Slip distribution of the 2005 Nias earthquake (Mw 8.6) inferred from geodetic and far-field tsunami data. *Geophysical Journal International*, *223*(2), 1162–1171. <https://doi.org/10.1093/gji/ggaa384>
- Gusman, A. R., Murotani, S., Satake, K., Heidarzadeh, M., Gunawan, E., Watada, S., & Schurr, B. (2015). Fault slip distribution of the 2014 Iquique, Chile, earthquake estimated from ocean-wide tsunami waveforms and GPS data. *Geophysical Research Letters*, *42*(4), 1053–1060. <https://doi.org/10.1002/2014GL062604>
- Hayes, G. P., Moore, G. L., Portner, D. E., Hearne, M., Flamme, H., Furtney, M., & Smoczyk, G. M. (2018). Slab2, a comprehensive subduction zone geometry model. *Science*, *362*(6410), 58–61. <https://doi.org/10.1126/science.aat4723>
- Heidarzadeh, M., & Satake, K. (2014). Possible sources of the tsunami observed in the northwestern Indian Ocean following the 2013 September 24 Mw 7.7 Pakistan inland earthquake. *Geophysical Journal International*, *199*(2), 752–766. <https://doi.org/10.1093/gji/ggu297>
- Kajiura, K. (1963). The leading wave of a tsunami. *Bulletin of the Earthquake Research Institute*, *41*(3), 535–571.
- Kornei, K. (2021). Ocean sensors record rare triple tsunamis near New Zealand. *Eos*, *102*. <https://doi.org/10.1029/2021EO157676>
- Lay, T., & Kanamori, H. (1980). Earthquake doublets in the Solomon Islands. *Physics of the Earth and Planetary Interiors*, *21*(4), 283–304. [https://doi.org/10.1016/0031-9201\(80\)90134-X](https://doi.org/10.1016/0031-9201(80)90134-X)
- Lockridge, P. A., & Lander, J. F. (1989). *United States tsunamis (including United States possessions): 1690-1988*. Homeland Security Digital Library; National Oceanic and Atmospheric Administration. Retrieved from <https://www.hSDL.org/?abstract&did=762302>
- Lorito, S., Romano, F., & Lay, T. (2016). Tsunamigenic major and great earthquakes (2004–2013): Source processes inverted from seismic, geodetic, and sea-level data. In R. A. Meyers (Ed.), *Encyclopedia of complexity and systems science* (pp. 1–52). Berlin, Heidelberg: Springer. https://doi.org/10.1007/978-3-642-27737-5_641-1
- Lundgren, P. R., Okal, E. A., & Wiens, D. A. (1989). Rupture characteristics of the 1982 Tonga and 1986 Kermadec earthquakes. *Journal of Geophysical Research: Solid Earth*, *94*(B11), 15521–15539. <https://doi.org/10.1029/JB094B11p15521>
- Macías, J., Castro, M. J., Ortega, S., Escalante, C., & González-Vida, J. M. (2017). Performance benchmarking of Tsunami-HySEA model for NTHMP's inundation mapping activities. *Pure and Applied Geophysics*, *174*(8), 3147–3183. <https://doi.org/10.1007/s00024-017-1583-1>
- Nikkhoo, M., & Walter, T. R. (2015). Triangular dislocation: An analytical, artefact-free solution. *Geophysical Journal International*, *201*(2), 1119–1141. <https://doi.org/10.1093/gji/ggv035>
- Piatanesi, A., & Lorito, S. (2007). Rupture process of the 2004 Sumatra–Andaman earthquake from tsunami waveform inversion. *Bulletin of the Seismological Society of America*, *97*(1A), S223–S231. <https://doi.org/10.1785/0120050627>
- Power, W., Wallace, L., Wang, X., & Reyners, M. (2012). Tsunami hazard posed to New Zealand by the Kermadec and Southern New Hebrides subduction margins: An assessment based on plate boundary kinematics, interseismic coupling, and historical seismicity. *Pure and Applied Geophysics*, *169*(1), 1–36. <https://doi.org/10.1007/s00024-011-0299-x>
- Romano, F., Lorito, S., Lay, T., Piatanesi, A., Volpe, M., Murphy, S., & Tonini, R. (2020). Benchmarking the optimal time alignment of tsunami waveforms in nonlinear joint inversions for the Mw 8.8 2010 Maule (Chile) earthquake. *Frontiers of Earth Science*, *8*. <https://doi.org/10.3389/feart.2020.585429>
- Romano, F., Lorito, S., Piatanesi, A., & Lay, T. (2020). “Fifteen years of (major to great) tsunamigenic earthquakes” in reference module in earth systems and environmental sciences. New York: Elsevier. <https://doi.org/10.1016/B978-0-12-409548-9.11767-1>
- Romano, F., Molinari, I., Lorito, S., & Piatanesi, A. (2015). Source of the 6 February 2013 $M_w = 8.0$ Santa Cruz Islands tsunami. *Natural Hazards and Earth System Sciences*, *15*(6), 1371–1379. <https://doi.org/10.5194/nhess-15-1371-2015>
- Romano, F., Piatanesi, A., Lorito, S., Tolomei, C., Atzori, S., & Murphy, S. (2016). Optimal time alignment of tide-gauge tsunami waveforms in nonlinear inversions: Application to the 2015 Illapel (Chile) earthquake. *Geophysical Research Letters*, *43*(21), 11226–11235. <https://doi.org/10.1002/2016GL071310>
- Rothman, D. H. (1986). Automatic estimation of large residual statics corrections. *GEOPHYSICS*, *51*(2), 332–346. <https://doi.org/10.1190/1.1442092>
- Satake, K. (2014). Tsunamis, inverse problem of. In R. A. Meyers (Ed.), *Encyclopedia of complexity and systems science* (pp. 1–20). Berlin, Heidelberg: Springer. https://doi.org/10.1007/978-3-642-27737-5_570-2

- Strasser, F. O., Arango, M. C., & Bommer, J. J. (2010). Scaling of the source dimensions of interface and intraslab subduction-zone earthquakes with moment magnitude. *Seismological Research Letters*, *81*(6), 941–950. <https://doi.org/10.1785/gssrl.81.6.941>
- Tanioka, Y., & Satake, K. (1996). Tsunami generation by horizontal displacement of ocean bottom. *Geophysical Research Letters*, *23*(8), 861–864. <https://doi.org/10.1029/96GL00736>
- Todd, E. K., & Lay, T. (2013). The 2011 Northern Kermadec earthquake doublet and subduction zone faulting interactions. *Journal of Geophysical Research: Solid Earth*, *118*(1), 249–261. <https://doi.org/10.1029/2012JB009711>
- Tsai, V. C., Ampuero, J.-P., Kanamori, H., & Stevenson, D. J. (2013). Estimating the effect of Earth elasticity and variable water density on tsunami speeds. *Geophysical Research Letters*, *40*(3), 492–496. <https://doi.org/10.1002/grl.50147>
- Watada, S., Kusumoto, S., & Satake, K. (2014). Traveltime delay and initial phase reversal of distant tsunamis coupled with the self-gravitating elastic Earth. *Journal of Geophysical Research: Solid Earth*, *119*(5), 4287–4310. <https://doi.org/10.1002/2013JB010841>
- Wetzler, N., Lay, T., Brodsky, E. E., & Kanamori, H. (2018). Systematic deficiency of aftershocks in areas of high coseismic slip for large subduction zone earthquakes. *Science Advances*, *4*(2), eaao3225. <https://doi.org/10.1126/sciadv.aao3225>
- Williamson, A., Newman, A., & Cummins, P. (2017). Reconstruction of coseismic slip from the 2015 Illapel earthquake using combined geodetic and tsunami waveform data. *Journal of Geophysical Research: Solid Earth*, *122*(3), 2119–2130. <https://doi.org/10.1002/2016JB013883>